Left ventricle Hermite-based segmentation

Jimena Olveres [a],[*], Rodrigo Nava [b], Boris Escalante-Ramírez [a], Enrique Vallejo [c], Jan Kybic [b]

[a] *Facultad de Ingeniería, Universidad Nacional Autónoma de México, Mexico*
[b] *Faculty of Electrical Engineering, Czech Technical University in Prague, Czech Republic*
[c] *Centro Médico ABC, Mexico*

ARTICLE INFO

ABSTRACT

In recent years, computed tomography (CT) has become a standard technique in cardiac imaging because it provides detailed information that may facilitate the diagnosis of the conditions that interfere with correct heart function. However, CT-based cardiac diagnosis requires manual segmentation of heart cavities, which is a difficult and time-consuming task. Thus, in this paper, we propose a novel technique to segment endocardium and epicardium boundaries based on a 2D approach. The proposal computes relevant information of the left ventricle and its adjacent structures using the Hermite transform. The novelty of the work is that the information is combined with active shape models and level sets to improve the segmentation. Our database consists of mid-third slices selected from 28 volumes manually segmented by expert physicians. The segmentation is assessed using Dice coefficient and Hausdorff distance. In addition, we introduce a novel metric called Ray Feature error to evaluate our method. The results show that the proposal accurately discriminates cardiac tissue. Thus, it may be a useful tool for supporting heart disease diagnosis and tailoring treatments.

1. Introduction

According to the World Health Organization, cardiovascular diseases rank number one as cause of death worldwide and were responsible for 31% of all deaths in 2012 [1]. Regarding heart failure, although it is a serious condition, it does not necessarily mean cardiac arrest. Tobacco, unhealthy diet, and obesity represent major risk factors for heart failure [2]. About 5.7 million adults in the United States have suffered from heart failure and about half of the people who develop heart failure die within 5 years of diagnosis [3]. Every year, approximately 500,000 new heart failure cases are diagnosed; this represents an estimated cost of $30.7 billion in health care [4].

In the case of left ventricular systolic dysfunction, the most pressing consideration is to determine if coronary artery disease, valvular disease, or any other etiology is responsible [5]. Whenever heart failure occurs, the heart shows reduced function. This may cause the left ventricle (LV) to lose its ability to contract or relax normally. In response, LV compensates for this stress by modifying its behavior, which creates hypertrophy that causes enlargement and hardening of the LV muscles and progresses to congestive heart failure [6].

Non-invasive imaging checkups and clinical controls increase the probability of the survival of patients. They are also very important in the initial assessment of patients with new-onset heart failure [7].

Information about the current condition of the anatomical structures of the heart is needed for an early and accurate diagnosis. In the case of suspected heart failure, the most common image modality is the ultrasound-echocardiography due to its low cost and good spatial resolution. However, the reproducibility of quantitative measurements is user dependent and can be variable [5]. Magnetic resonance imaging (MRI) has also been used as a reference method [8]. It is useful for scanning and detecting abnormalities in soft organs and there is no involvement of any kind of radiation, yet it is expensive and presents limited availability compared with computed tomography (CT) [9].

In the case of heart failure along with coronary artery disease, CT imaging provides insights and detailed information of the heart that support and tailor treatments. Furthermore, heart examination using CT generates 2D and 3D high-resolution images throughout the entire cardiac cycle, which are useful for segmentation tasks. Although CT imaging does not provide suitable contrast resolution in comparison with MRI, it is more accessible and has enough spatial resolution to distinguish adjacent organs [10]. In addition, the use of contrast agents can improve endocardial border definition.

Cardiac segmentation is still a challenging task due to biological aspects that depend on the diverse organ anatomy and physical issues that image modalities must face. These include for example, noise due to unwanted movements, also from the respiratory system, cardiac

---

* Corresponding author.
  E-mail address: jolveres@uxmcc2.iimas.unam.mx (J. Olveres).

synchronization, and differences in anatomy when a pathology occurs.

As a prerequisite for LV visualization, the heart must be oriented in order to obtain a canonical view: horizontal, long, and short axis views. The short axis view shows a plane that is perpendicular to the long axis and gives a suitable cross-sectional view of both ventricles [11,12]. On the short axis view, LV is displayed as an alignment from the base of the heart to the apex, see Fig. 1.

1.1. Related work

Several techniques have been developed for epicardium and endocardium segmentation using the short axis view. Petitjean and Dacher [13] presented a review of a large group of automated and semi-automated segmentation methods. The review includes methods based on atlases, deformable models such as level sets (LS) and statistical models with prior knowledge such as active shape models (ASM). However, these methods are focused on MRI. Kang et al. [8] also wrote a review about the most used methods in cardiac segmentation. However, classic active contours and level sets are associated with a minimum functional, which often leads to over-segmentation [14].

It is well-known that CT-based heart segmentation is sensitive to initialization, noise, and image characteristics. Therefore, other studies have suggested that the combination of different techniques may improve organ segmentation [15,16,17,18]. For instance, in Ref. [19], the authors improved the weighted C-means clustering [20] with a fitting model. In Ref. [18], Kronman et al. proposed an adjustment to the segmentation by using active contours based on level sets and a correction of the segmentation leaks using a ray casting method. Ma et al. [21] used a Haar classifier to detect the heart area. Then, the segmentation is performed with an ASM. Dolz et al. [22] showed a hybrid approach combining a watershed transformation with graph-cut segmentation in order to delineate organs such as the spinal canal, lungs, heart, and pericardium. Antunes et al. [23] used level sets to extract the cardiac surface from multi-detector computed tomographic data. The authors coupled a 3D level set with a stopping function based on a multi-scale second derivative Gaussian filter. The results show that the combination of methods outperforms single approaches.

Local binary patterns (LBPs) have proven to be a suitable tool when they are used in combination with active contours because LBPs are able to model local structures in a robust way against illumination changes, while ASMs take advantage of the velocity of local variations to localize landmarks [24]. Features such as texture, color, or morphology should be included in a deeper analysis in order to enhance the performance of the final segmentation (e.g. in Olveres et al. [25] an application to

Fig. 1. CT image of the heart displayed using the short axis view where it is possible to see the right and left ventricles. The red ellipse defines the endocardium, whereas the blue ellipse defines epicardium. This segmentation resembles typical boundaries drawn by clinicians. (For interpretation of the references to colour in this figure legend, the reader is referred to the web version of this article.)

mesencephalon segmentation).

On the other hand, methods that resemble the human visual system have increased in popularity because they allow images to expand into a local decomposition that describes intrinsic attributes related to important cues and highlights structures that are useful for segmentation [26]. The Hermite transform (HT) [27,28] has been used successfully as a texture descriptor in Refs. [29,30]. HT is a special case of the Polynomial transform and is based on Gaussian derivatives, thus, it is possible to compute local orientation analysis.

1.2. Contribution

We propose a novel strategy to segment LV boundaries with better precision. The proposal combines information from HT with ASM and LS. Hence, it is possible to take advantage of the relevant perceptual information of the LV and its adjacent structures to improve the segmentation. The procedure considers endocardium (inner wall) and epicardium (outer wall) delineations. Although papillary muscles are typically excluded in standard studies, we also consider them in the segmentation approach. This consideration may allow us to measure more precisely the total volume of blood throughout the entire cardiac cycle [31]. We conduct several evaluations using different criteria such as Dice coefficient and Hausdorff distance. We also introduce a novel metric called Ray Feature error (see Appendix A). Furthermore, we include a comparison between our proposal and different schemes based on ASMs, LBPs, and LS.

The remainder of the paper is organized as follows: Section 2 presents the mathematical foundations used in this proposal based on ASMs and a deformable model known as fast level set (FLS). In Section 3 the proposal is introduced, in Section 4 the dataset is described, in Section 5 the experiments are shown, while in Section 6 a discussion is presented. Finally, Section 7 concludes the paper addressing unsolved challenging problems.

2. Theoretical background

2.1. Active shape models

Cootes et al. [32] proposed ASMs as a refinement of the statistical deformable models. An ASM consists of an average shape, $\overline{X}$, that is derived from a point distribution model (PDM). The goal of the approach is based on the idea that it is possible to deform $\overline{X}$ to some extent in order to produce certain variability until the ASM meets the boundaries of the object of interest. The algorithm is divided into the following steps:

(i) A set of M aligned shapes is built. For each training shape, a vector of landmarks is obtained: $S_i = \{(x_0,y_0), \ldots, (x_{i-1},y_{i-1})\}^T$. So that, the mean shape, $\overline{X}$, is the average of all landmarks $\overline{X} = \frac{1}{M}\sum_{k=0}^{M-1} S_k$.

(ii) The variations of the mean shape are obtained by computing principal component analysis [32]. The mean shape is deformed within certain limits to recognize a new shape according to $\widehat{X} = \overline{X} + P\boldsymbol{b}$, where P is the matrix of the t first principal components, $\boldsymbol{b}$ is the weight vector, and $\widehat{X}$ is the estimated shape.

(iii) $\overline{X}$ is placed close to the object of interest manually. Each landmark in $\overline{X}$ is compared with its corresponding gray level profile, which is a line of pixels perpendicular to the landmark. In this moment, the algorithm includes a gray-level model that moves the landmarks iteratively according to an optimization criterion based on distances from the desired contour.

It is well-known that ASMs are often limited when dealing with texture segmentation because they model contours using only shape. Typically, gray level information is included in the functional that drives the fitting of the contour. In contrast, Active Appearance Model (AAM) proposes an alternative to represent contours using shape and texture
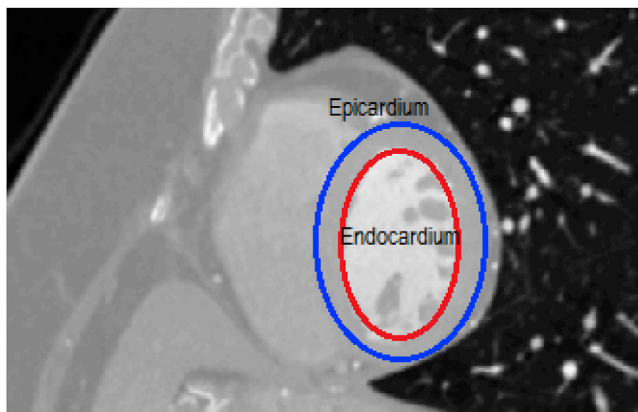
parameters. Similarly to ASM, the joint model is constructed with eigenvalue analysis, however, this is more complicated and time consuming than an only-shape-based approach because it requires training. In our ASM proposal, texture characterization is computed using either Hermite coefficients or LBPs, and included within the functional that drives the contour. It is easier and faster to include texture information in a functional than in a parametric model because the functional does not need training [33,34].

2.2. Deformable models based on level sets

Nowadays, a multitude of deformable models based on level sets exists in the literature. However, Chan-Vese [35] is one of the best known algorithms because it is a powerful and flexible method that is able to segment many types of images even when an image does not contain well-defined boundaries. The aim of the Chan-Vese model is to minimize an energy functional and find the partition C that forms a border between two regions of interest in u_0, where u_0 is an image defined as: $u_0 : \Omega \rightarrow \mathbb{R}$.

An extension of this model is the so-called vector-value model [36] where complimentary information of the image is included to obtain a better segmentation. This model minimizes the energy functional using the Euler-Lagrange equation:

$$\frac{\partial \phi}{\partial t} = \delta_e \left[\mu \text{div} \left(\frac{\nabla \phi}{|\nabla \phi|} \right) - \frac{1}{N} \sum_{i=1}^{N} \lambda_i^+ \left(u_{0,i} - c_i^+ \right)^2 + \frac{1}{N} \sum_{i=1}^{N} \lambda_i^- \left(u_{0,i} - c_i^- \right)^2 \right]$$

(1)

where c^+ and c^- are constant vectors that represent the average value of u_0 inside and outside the curve C, respectively. μ and $\lambda^{+,-}$ allow us to tune the detector's sensitivity. However, this method is computationally demanding [37,38].

In this paper, we use a model called fast level set (FLS) [39] that is a variation of the classic Chan-Vese algorithm. FLS aims to improve performance and reduce computational complexity by avoiding the iterative solution of the partial differential equation, Eq. (1). It has a simple discrete representation that reduces computational complexity. The idea of FLS is to represent the zero level set as a list of boundary points that moves towards a discrete edge without computing Eq. (1). At the same time, FLS mantains the advantages of traditional methods.

Further simplifications develop from the fact that the evolution of FLS needs binary information that evolves into a speed function $v(x)$ as follows:

$$v(x) = \begin{cases} 1 & \text{if } -\lambda_1 (f(x) - c_1)^2 + \lambda_2 (f(x) - c_2)^2 \geq 0 \\ -1 & \text{if } -\lambda_1 (f(x) - c_1)^2 + \lambda_2 (f(x) - c_2)^2 < 0 \end{cases}$$

(2)

The algorithm includes a regularization phase with an anisotropic Gaussian filter applied to the level set function. FLS is a reliable algorithm. However, its main drawback is that the initial region must be well-defined in order to create the original speed. In some cases, LS algorithms generate shapes with inconsistent topology, with respect to the actual object, when they are applied to noisy images [40]. To overcome this situation, we use additional information given by the Hermite coefficients, as a vector value model, to improve the definition of the regions.

2.3. Steered Hermite transform

Over the last decades, many computational methods have incorporated simple biological properties of vision. One example is the Hermite transform [27] that it allows to perform local orientation analysis by windowing an image with a Gaussian function. On each window position, an expansion using orthogonal polynomials is calculated in order to obtain the Hermite coefficients (HCs).

The importance of HT relies on the fact that it mimics some of the most important characteristics of the human visual system such as the Gaussian receptive fields and the Gaussian derivative model of early vision. The HT is useful to extract relevant image structures efficiently [41,42].

HT is associated with a class of orthogonal polynomials called Hermite polynomials, $H_n(x)$, defined as follows:

$$H_n(x) = (-1)^n e^{x^2} \frac{d^n \left(e^{-x^2} \right)}{dx^n}$$

(3)

where n denotes the order of the polynomial.

The Cartesian Hermite coefficients, $L_{n-m,m}$, can be directly obtained by convolving the image, $I(x, y)$, with the Hermite analysis functions, D_n (see Fig. 2(a)) as follows:

$$L_{n-m,m}(x_0, y_0) = \int \int I(x, y) D_{n-m,m}(x_0 - x, y_0 - y) dx dy$$

(4)

with $D_n(x) = H_n(x) \cdot G^2(x)$ where $G^2(x)$ represents a Gaussian function.

The steered Hermite transform (SHT) is derived from a linear combination of rotated Cartesian Hermite coefficients [43] (see Fig. 2(b)). The rotation follows a maximum energy criterion [26]. SHT produces a new and reduced set of coefficients that are oriented over an angle θ:

$$L_{m,n-m,\theta}(x_0, y_0) = \sum_{k=0}^{n} L_{k,n-k}(x_0, y_0) R_{k,n-k}(\theta)$$

(5)

where $R_{m,n-m}(\theta) = \sqrt{\binom{n}{m}} \cos^m(\theta) \sin^{n-m}(\theta)$.

SHT has proven to be effective in texture analysis [43,26]. It is well suited for multi-resolution analysis and can be implemented as a fast algorithm [43].

3. The proposed method

The goal of this study is to identify endocardial and epicardial walls that contain myocardium with better precision. In the dataset, the endocardium possesses good contrast, while the epicardium is not always well-defined. Several attempts to segment such structures have been made but still better techniques are needed to improve results. We suggest taking advantage of the SHT to characterize important tissue structures and incorporate the information into the ASMs and LS schemes to improve the segmentation. A block diagram resumes the proposal in Fig. 3.

The first step is to seed suitable initialization for the ASM and LS algorithms. This is accomplished by estimating the position of the centroid of the LV blood pool during the diastole phase using a compactness metric similar to Lu et al. [15], (see Fig. 4). This is a simple yet effective way to compute the initial pose. We perform this step on a slice from the mid-third or mid-cavity of the heart volume [44,45]. A limitation of this step is that in the case of failure the LV cavity center must be manually specified.

3.1. Combining active shape models

In Ref. [46], the authors proposed to combine ASMs and LBPs by considering only landmark profiles (see Fig. 5(a)). Here, we extend the area of analysis and propose to combine ASMs with LBPs, and ASMs with HCs to improve the segmentation of the LV. In addition, we made changes to the original ASM algorithm and four methods are explored.

For all the cases, the initial parameters are set to: number of landmarks = 70, normal profile length = 11, and iterations = 60. These values were chosen based on the results of the experiments. We evaluated different combinations of the number of landmarks, profile length, and number of iterations. In the case of our level sets approach we used 60 iterations, based on the reported performance for each error index.

3.1.1. ASM/Quadratic-LBP (ASM/LBP)

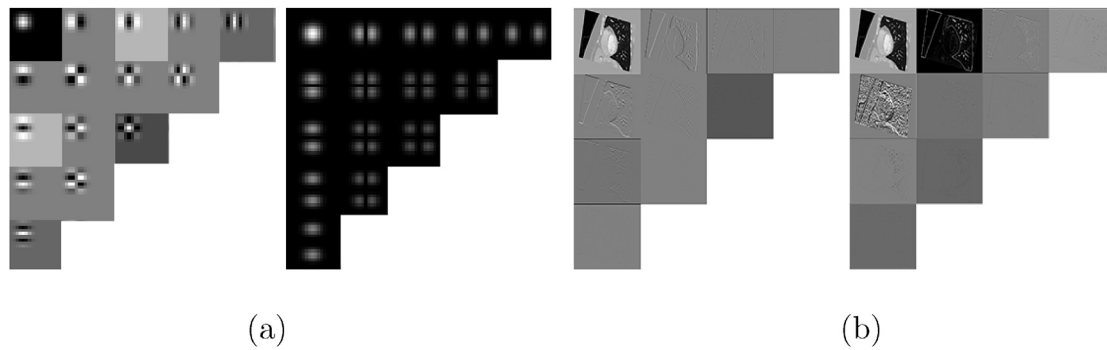During the training phase, the LBPs are calculated over four square

Fig. 2. (a) Ensemble of spatial Hermite filters (left) and their corresponding frequency responses (right). We display orders from $N = 0$ to $N = 4$. (b) Cartesian (left) and steered Hermite coefficients (right). Note that the energy is concentrated in the upper row of the steered Hermite coefficients.
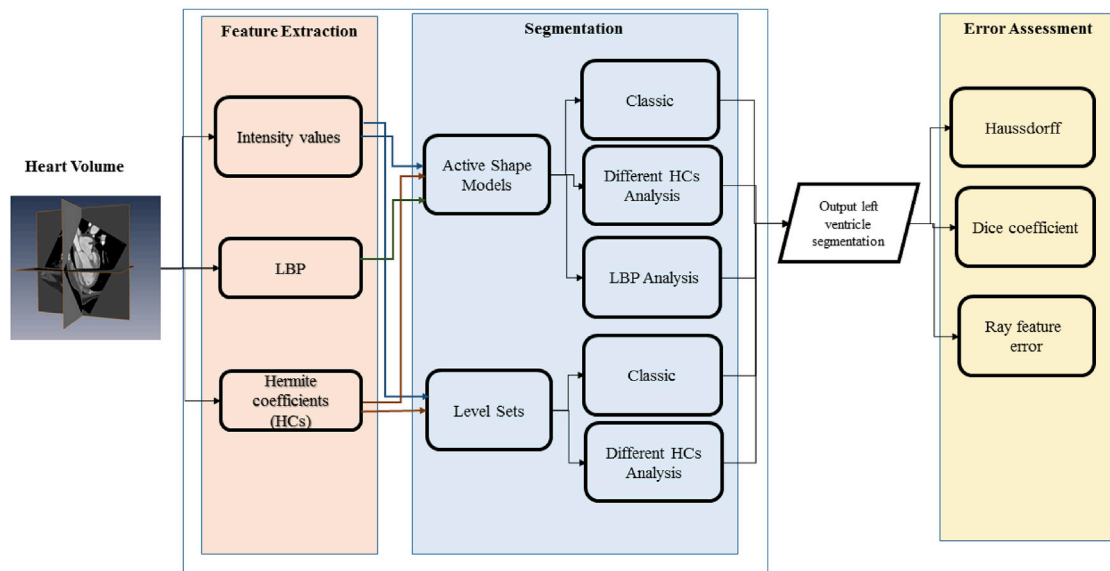

Fig. 3. Overview of the experiments conducted in this study. First, feature extraction is performed and then incorporated into both ASMs and LS methods to improve segmentation of cardiac walls. The assessment is conducted with three metrics: Hausdorff, Dice, and, Ray Feature error.

regions of 5×5 pixels around every landmark based on the approach presented in Ref. [46]. Then, a histogram that describes the corresponding landmark is constructed by concatenating the four local histograms (see Fig. 5(b)). LBP is a simple but powerful method to characterize textures. Despite the fact there are quite a few versions [47], we opted here for the original LBP due to its good performance and simplicity.

The histograms obtained during the recognition phase are compared against the trained histograms of the corresponding landmarks, so that, the closest point to the boundary is the one with the smallest histogram distance. We used the Chi-square distance. This distance can be used as a measure of dissimilarity between distributions, specifically between two histograms. It has also been used in applications such as texture and object classification and image retrieval [48]. A diagram with the description of the method is shown in Fig. 5.

3.1.2. ASM/HCs

First, the HCs are computed with Eq. (5) and incorporated into the ASM in a multi-spectral fashion. Namely, every steered Hermite coefficient vector $\{L_k | k = 0, \ldots, 3\}$ is considered a multi-spectral band. Thus, the multi-spectral values of the landmarks and profiles, g_i, are defined as follows:

$$g_i = \left[g_{pL_0}\left(x_p, y_p : L_0\right), g_{pL_1}\left(x_p, y_p : L_1\right), g_{pL_2}\left(x_p, y_p : L_2\right), g_{pL_3}\left(x_p, y_p : L_3\right) \right]$$

(6)

where g_{pL_k} are the gray values at the position (x_p, y_p) that correspond to the profile p of the Hermite coefficients $L_0, \ L_1 \ L_2, \ $ and L_3 respectively. Here, we use the Mahalanobis distance to calculate the closest point to each landmark.

3.1.3. ASM/Profile-HCs (ASM/PHCs)

Similar to ASM/LBP, for every landmark and its corresponding profile, the HCs are computed over a 9×9 pixel window (see Fig. 6). The Hermite coefficients are computed only around the landmarks in order to speed up the process. The final histogram is created by concatenating the histograms of the HCs as follows:

$$p(r_{kL_n}) = \frac{1}{MN}\{n_{kL_0}, \ n_{kL_1}, \ n_{kL_2}, \ n_{kL_3}\}$$

(7)

where n_k represents a k-bin histogram of the Hermite coefficients L_0, $L_1 \ L_2, \ $ and L_3 that correspond to the profile p. r_{kL_n} is the final histogram of the L_n coefficients that is normalized by the size of the image M (rows) and N (cols). Finally, the landmark position is adjusted by computing the smallest distance between the searched landmark's histogram and the
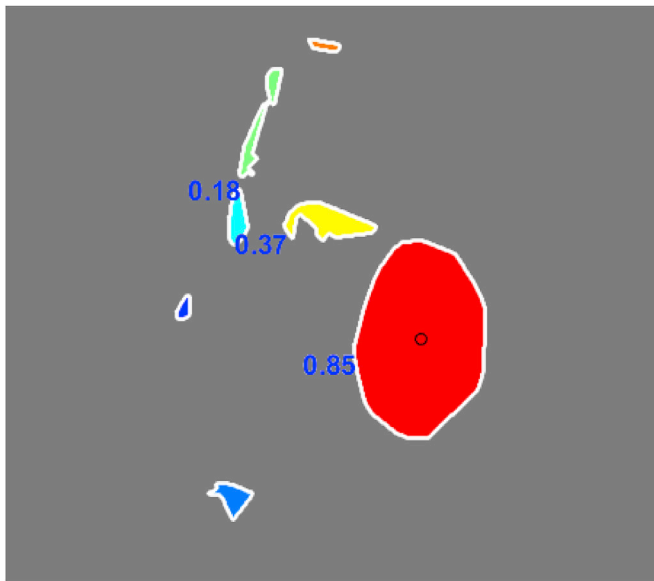
Fig. 4. Metric of compactness. The blue numbers indicate the compactness value. A value of 1 means that the shape of the object is closer to a circle. During this step, the object with the largest compactness value is retained. (For interpretation of the references to colour in this figure legend, the reader is referred to the web version of this article.)

profile's histograms of the new image according to the Chi-squared function.

3.1.4. ASM/Quadratic-HCs (ASM/QHCs)

Here, we propose to compute HCs over four square regions defined by a 7×7 pixel window around the landmarks. This is similar to the quadratic region used in ASM/LBP (see Fig. 7) but here the information from the HCs L_0, L_1 L_2, and L_3 is included.

$$p(r_{QkL_n}) = \frac{1}{MN} \{n_{QkL_0},\ n_{QkL_1},\ n_{QkL_2},\ n_{QkL_3}\} \tag{8}$$

where Q stands for quadratic region.

3.2. Combining fast level sets

Level sets are an efficient method for segmenting organ tissue when the borders possess good contrast (e. g. endocardium). However, the main bottleneck is the computation time. Thus, we use fast level sets in combination with the Hermite coefficients. After testing several iteration values, we studied the behavior of the number of iterations against the error indexes in order to obtain the best value. The final value for the number of iterations is 60.
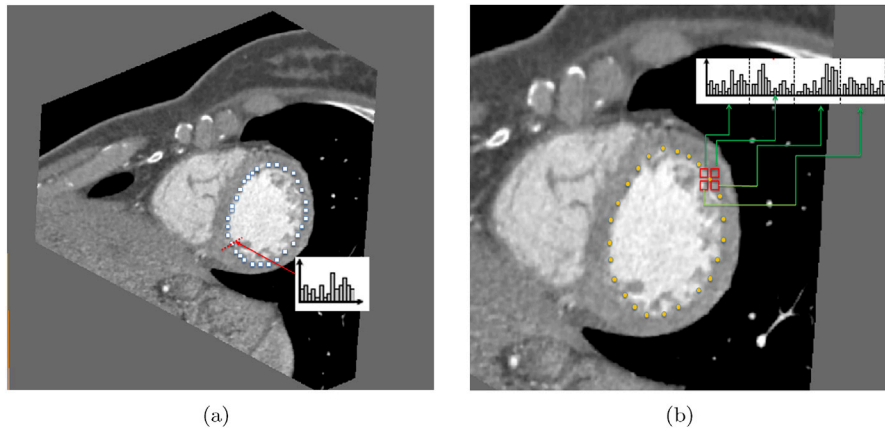

(a)

(b)

Fig. 5. Two different techniques to combine ASMs and LBPs. (a) For every landmark, the LBP histograms are computed on all points of the corresponding profile of length *n*. (b) Quadratic-LBP histogram computes LBPs on four square regions of 5×5 pixels around each landmark, then a histogram is built by concatenating the four local histograms one after another.
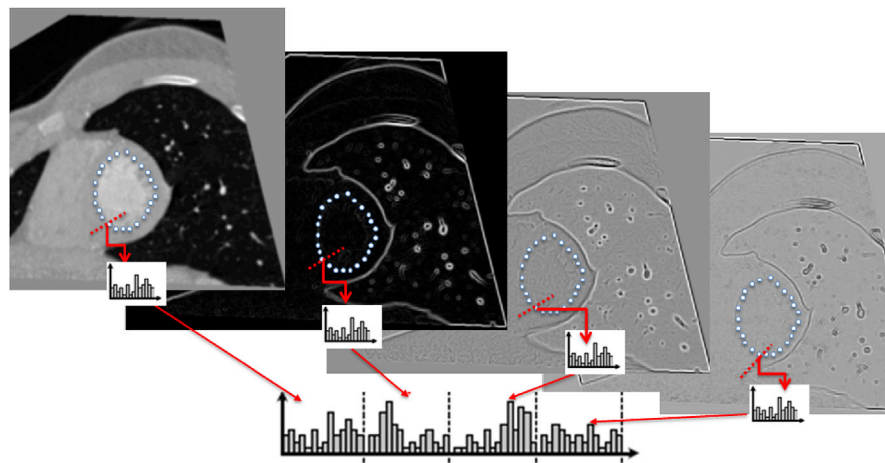

Fig. 6. ASM/Profile-HCs scheme. The diagram shows the construction of the histograms for each landmark. For a given point in a profile, the four histograms of the corresponding Hermite coefficients are concatenated.
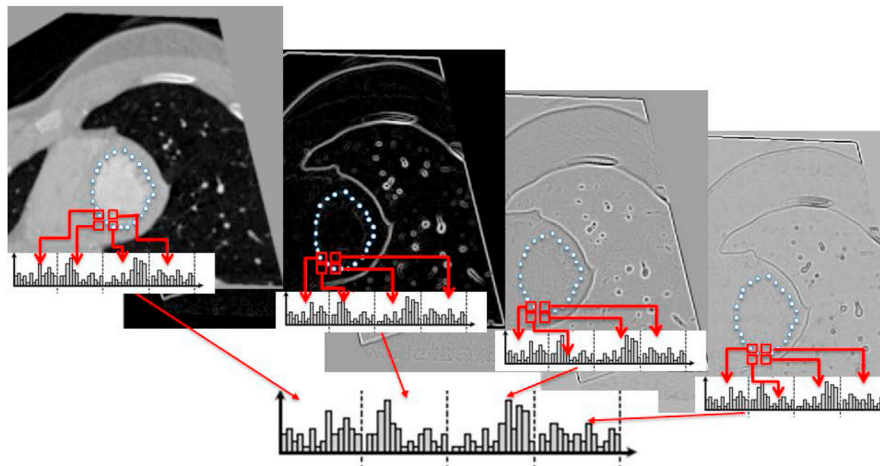
Fig. 7. ASM/Quadratic-HCs scheme. The diagram shows the construction of the histogram. For a given point, four regions around a landmark are computed. This procedure is performed on every Hermite coefficient.

3.2.1. FLS/HCs

The steered Hermite coefficients are used as a simplified vector model that defines the initial velocity field as follows:

$$
\frac{\partial \phi}{\partial t} = \delta_e \left[\mu \mathrm{div} \left(\frac{\nabla \phi}{|\nabla \phi|} \right) - \frac{1}{4} \left\{ \lambda_0^+ \left(L_0 - c_0^+ \right)^2 + \lambda_1^+ \left(L_1 - c_1^+ \right)^2 \right. \right.
$$
$$
\left. + \lambda_2^+ \left(L_2 - c_2^+ \right)^2 + \lambda_3^+ \left(L_3 - c_3^+ \right)^2 \right\} + \frac{1}{4} \left\{ \lambda_0^- \left(L_0 - c_0^- \right)^2 \right.
$$
$$
\left. \left. + \lambda_1^- \left(L_1 - c_1^- \right)^2 + \lambda_2^- \left(L_2 - c_2^- \right)^2 + \lambda_3^- \left(L_3 - c_3^- \right)^2 \right\} \right] \quad (9)
$$

where L_x are the HCs, c_x^- and c_x^+ are the average values inside and outside the curve respectively.

4. Materials

A dataset of 28 annotated tomographic cardiac studies was acquired from healthy subjects with a CT Siemens dual source scanner (128 channels) at Hospital Ángeles Pedregal México. The heart volumes were captured in signed 12-bits DICOM format. The age of subjects range from 17 to 81 with an average age of 55. 16 studies belong to males and 12 studies belong to females. All patients present low risk for coronary artery disease and atypical chest pain.

Each study belongs to a single subject and consists of 10 vol taken at different times during the electrocardiography (ECG)-synchronized cardiac cycle. This method is called ECG-gating, where a volume is acquired only during certain consecutive period of the cardiac cycle being retrospectively reconstructed. It covers systolic and diastolic cardiac phases.

Our studies start on a final diastolic (relaxing) phase, go throughout the systolic (contraction) phase and return to the diastolic phase, providing images at 0%, 10%, 20%, 30%, 40%, 50%, 60%, 70%, 80% and 90% of the cardiac cycle. The spatial resolution values range from $0.302734 \times 0.302735 \times 1.5$ [mm] to $0.433593 \times 0.433593 \times 1$ [mm].

Since the volumes are oriented on different angles, a manual alignment with the short axis view was performed. This step was reviewed by experienced physicians. Furthermore, due to the fact that modern CT scanners have a wide range of Hounsfield units (HU), the volumes were mapped into a more suitable range from -1024 HU to 2200 HU. Then, a normalization step was applied to avoid negative values.

5. Experimental results

The aforementioned algorithms were validated against manual annotations made by an expert physician and one assistant in 28 studies throughout the entire cardiac cycle from healthy subjects. We used the middle slices of the volumes, so that every study is composed of ten images that cover diastole and systole phases. We also identified each slice with the percentage of the cardiac cycle [0%, 10%, 20%, …, 90%]. A total of 280 different images were tested on a 2D slice-by-slice scheme. For the proposed initialization, we obtained good results on 22 of the 28 slices. The evaluation started with images at 0% cardiac cycle per subject. The same initialization was used throughout the cycle.

In order to reduce bias, we used four-fold cross-validation to train the ASM. Every fold was chosen randomly. Our experiments were divided into two groups: endocardium (Section 5.1) and epicardium segmentation (Section 5.2).

The experiments with FLS include an expansion of the resulting contour that encloses the cavity segmentation. The procedure segments papillary muscles followed by a convex hull in order to generate a rounded envelope to enfold them. This step represents a refinement that allows the segmentation to resemble boundaries manually drawn by clinicians.

Regarding epicardium segmentation, an example using ASMs is shown in Fig. 8(a). The experimental contour in blue is compared against the ground-truth boundary in red. With respect to the steered Hermite coefficient computation, different window sizes were evaluated. A window size of 9×9 pixels achieved better quantitative results in most of the cases, including the endocardium wall (see Fig. 8(b) where papillary muscles are also segmented in yellow.)

We performed a quantitative analysis using three metrics: Hausdorff distance (HD), Dice index (DI), and Ray Feature error (RFE). The latter is a novel metric for segmentation evaluation based on ray features [49]. It allows us to measure in a simple, robust way shape similarities between two overlapping objects. The method is introduced in Appendix A. Examples of the best segmentations for endocardium and epicardium are shown in Fig. 8.

In order to evaluate the segmentation performance of the different approaches presented, we ran ANOVA analysis. The p-values are shown in Figs. 10 and 11 for endocardium and pericardium respectively.

5.1. Endocardium segmentation

In order to segment the endocardium, seven different schemes were computed. Two methods are based on fast level sets, FLS and FLS/HCs, and the rest of the methods are based on ASMs: ASM, ASM/HCs, ASM/PHCs, ASM/QHCs, and ASM/LBP. As expected, segmentation during systole is a more challenging task but it can be observed that in most cases the best results were achieved with FLS and FLS/HCs, while ASM/LBP presented the worst result.

Since the performance of the level set-based algorithms strongly depends on the number of iterations, we include a comparison of the best
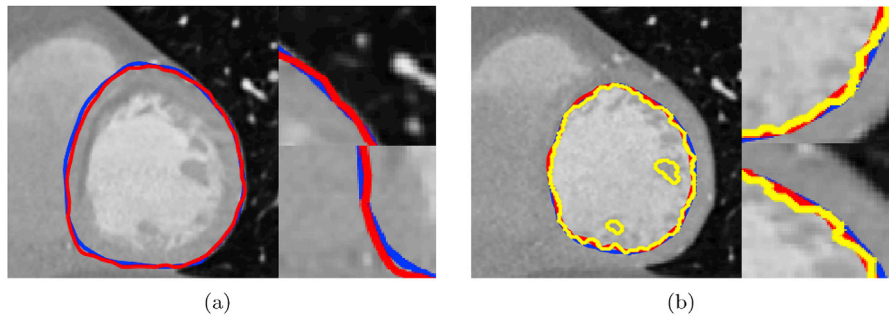
Fig. 8. Segmentation details. Ground-truth boundary (red), experimental segmentation (blue). The best segmentation cases for (a) ASM/QHCs on the epicardium and (b) FLS/HCs on the endocardium. Papillary muscles are delineated on yellow. (For interpretation of the references to colour in this figure legend, the reader is referred to the web version of this article.)
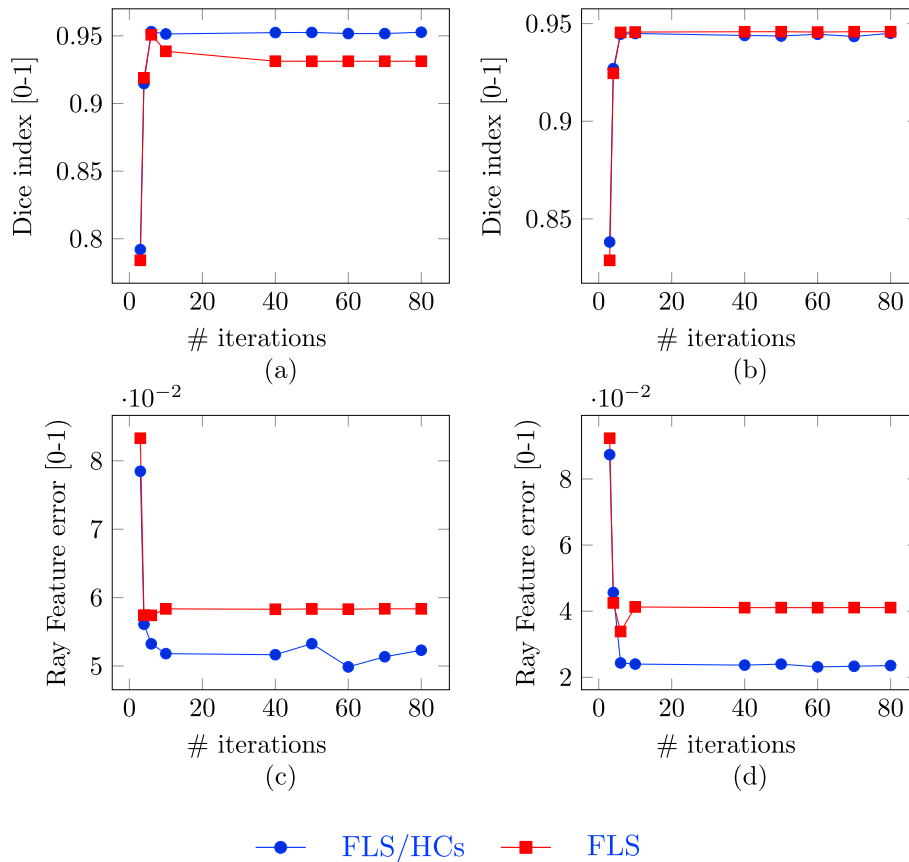

Fig. 9. Plots depict the performance of FLS and FLS/HCs endocardium segmentation against the number of iterations measured with Dice index (upper row) and Ray Feature error (lower row). Dice index is between 0 and 1, values close to 1 indicate similar contours. Ray Feature error is between 0 and 1; values close to 0 indicate similar contours. The values were taken during (a) 0%, (b) 60%, (c) 20%, and (d) 90% of the cardiac cycle.

two cases and their behavior when the number of iterations changes (see Fig. 9). Average results are summarized in Fig. 10 using HD, DI, and RFE. Note that RFE shows clearer differences among algorithms and seems more consistent with DI than with HD.

5.2. Epicardium segmentation

In order to segment epicardium, six approaches were computed: FLS/HCs, ASM, ASM/HCs, ASM/PHCs, ASM/QHCs, and ASM/LBP. In this section, FLS approach was not included because the algorithm did not converge due to the lack of contrast in the tissue that surrounds the epicardium.

In general, throughout the cardiac cycle the ASM-based methods show good results, especially those methods that include texture information like ASM/QHCs and in some percentages ASM/LBP, whereas

ASM/HCs achieved the poorest results. It is important to observe that FLS/HCS also presents good performance. The average results are summarized in Fig. 11. Also in this case, RFE is more consistent with DI than with HD. Consider for instance that HD changes the rank order of the best performing algorithms ASM, ASM/QHCs, and ASM/LBP throughout the cardiac cycle in comparison with DI and RFE.

Segmentation of the endocardium and the epicardium throughout the cardiac cycle is presented in Fig. 12.

5.3. Evaluation of segmentation under noisy images

In order to assess how the addition of Hermite coefficients adds robustness to the segmentation, the approaches FLS and FLS/HCs were evaluated in the endocardium segmentation by adding Gaussian noise with zero mean and incrementing the variance gradually. Comparison
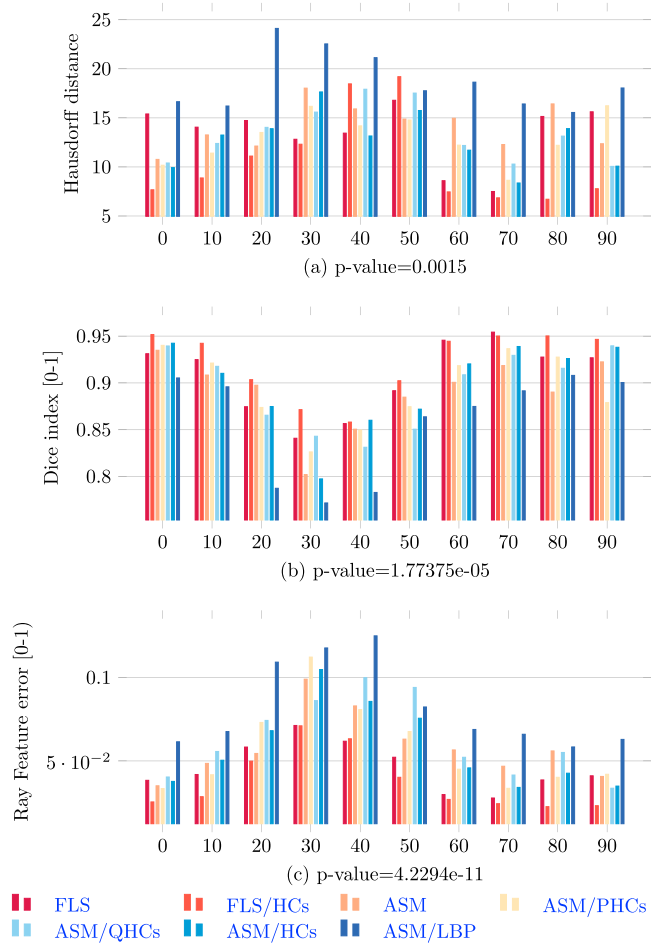
Fig. 10. Average distances between the experimental and the expert contours with Hausdorff distance (lower values indicate more alike boundaries), Dice coefficient (values close to 1 indicate more similar contours) and Ray Feature error (values close to 0 indicate more similar contours) for endocardium segmentation. X-axis represents the percentages of the cardiac cycle (diastole-systole).
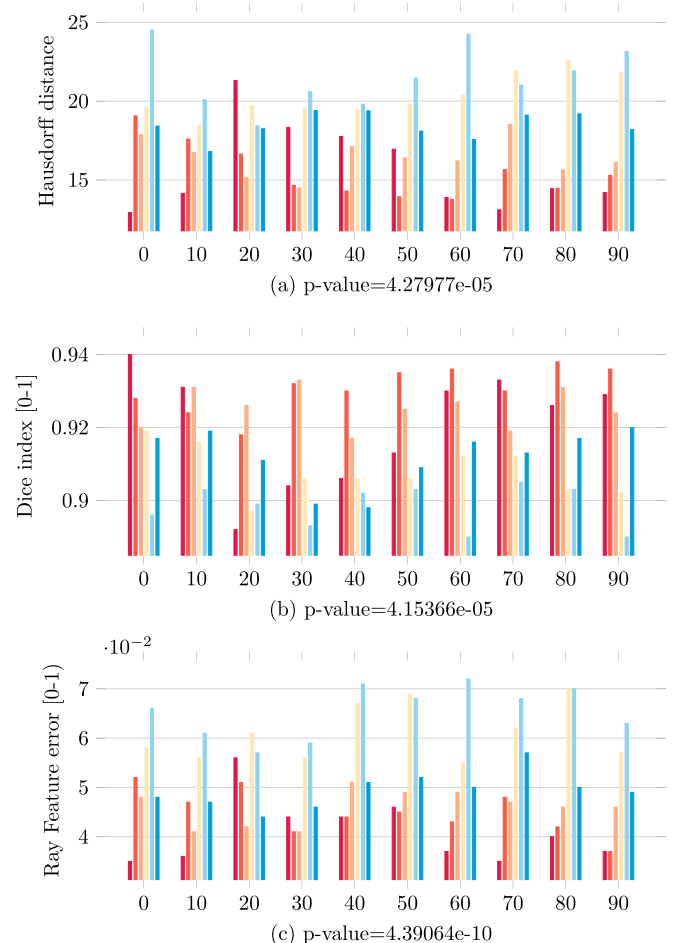

Fig. 11. Average distances between the experimental and the expert contours with Hausdorff distance (lower values indicate more alike boundaries), Dice coefficient (values close to 1 indicate more similar contours) and Ray Feature error (values close to 0 indicate more similar contours) for epicardium segmentation. X-axis represents the percentages during the cardiac cycle (diastole-systole).

results are shown in Fig. 13. Notice that FLS/HCs shows a better performance in comparison with FLS.

5.4. Volume segmentation

In spite of the fact that the proposal is performed in 2D, it is possible to reconstruct the heart volume from a set of slices that covers the whole left ventricle. This procedure may allow clinicians to measure important indices such as volume, mass, and ejection fraction. A 3D left ventricle reconstruction is presented in Fig. 14 using FLS/HCs.

5.5. Future clinical usability

In future studies, we will explore how to characterize heart failure pathologies based on segmentation patterns. Here, we present an initial test on a patient with infarction on the anterior wall, see Fig. 15. Note that the wall does not contract and expand as much as the rest of the myocardial tissue. We used the FLS/HCs algorithm, which achieved the best performance in this case, to segment epicardium and endocardium. From both segmentations the cardiomyopathy is clear, thickness of the anterior ventricular wall remains approximately constant along the cardiac cycle.

6. Discussion

From our results (see Figs. 9 and 10), we consider fast level sets in

combination with HCs as the first option when the endocardium is segmented. The reason is that the information provided by HCs improves the convergence and velocity of our method. The results remain consistent when comparing the three metrics: Dice, Hausdorff, and Ray Feature error.

The image expansion computed with the steered Hermite transform permits the extraction of features based on Gaussian derivatives that highlight salient visual cues. The SHT enhances segmentation because it adapts to local orientation content. The window of analysis used to compute the steered Hermite coefficients was set to 9×9. We also evaluated different sizes: 5×5, 7×7, and 11×11 with suboptimal results. However, the window size of analysis used in SHT is not related to the window used with LBPs because the approaches belong to a different analysis. The LBPs window size was previously evaluated in Ref. [46] where multiple variations of LBPs were studied. According to our results, the method ASM/QHCs outperforms ASM/LBP.

In the case of epicardium segmentation the lack of tissue contrast that surrounds the epicardium hampered the segmentation with FLS. Nevertheless, the joint model FLS/HCs converged in spite of the poor border definition. The combination of HCs and ASMs also enhanced the segmentation performance on the epicardium. Consequently, the limitation of the shape restriction inherent to the method was overcome. It is
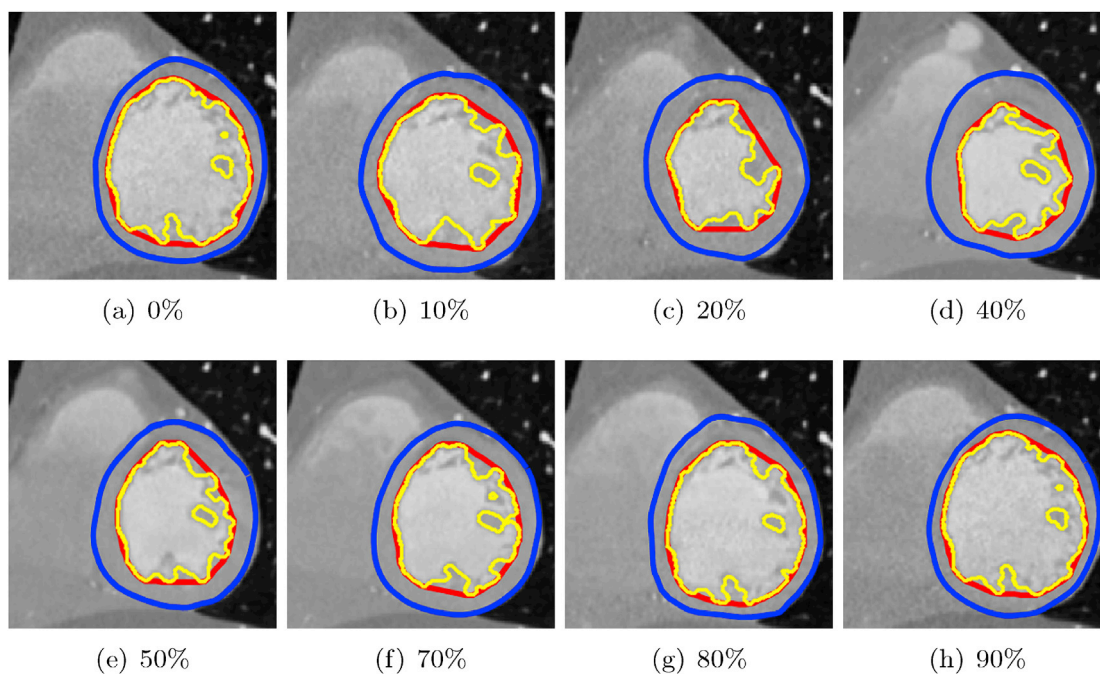
Fig. 12. Final segmentations of endocardium (red), epicardium (blue) and papillary muscles (yellow) throughout the cardiac cycle. (For interpretation of the references to colour in this figure legend, the reader is referred to the web version of this article.)
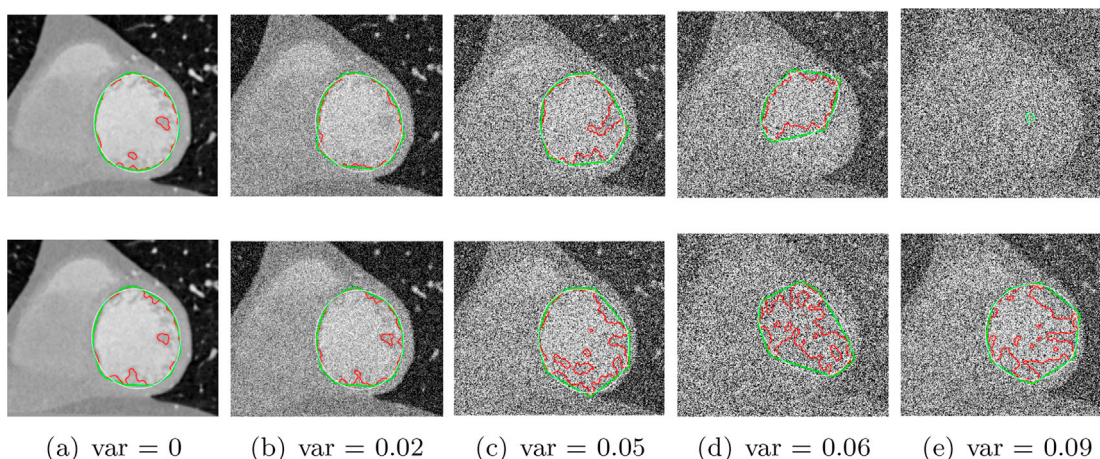

Fig. 13. Comparison of segmentation results between FLS (upper row) and FLS/HCs (lower row) on the endocardium (red contour) using zero mean and different variances (var). (For interpretation of the references to colour in this figure legend, the reader is referred to the web version of this article.)

important to mention that with other variations of ASMs, as in the case of adding Hermite coefficients and LBP information, the segmentation improved. When using approaches based on local features such as ASM/QHCs and ASM/LBP, the final results also achieved better segmentations, which suggests that including both local and global information may lead to better results.

From the endocardium results (see Fig. 10), it is possible to infer that the segmentation performance of all the methods varies along the cardiac cycle, with systole being the most difficult phase to segment. However, the algorithm rank performance remains with no changes. On the other hand, when attempting to segment the epicardium, contrast differences are low. This implies that in addition to the borders, texture information must be taken into account. The Hermite coefficients obtained from Gaussian derivative operators include relevant texture information and can therefore improve segmentation.

When ASM/QHCs was used for segmenting the epicardium, (see Fig. 11), the results obtained were consistent with good scores. ASM/LBP

ranks in the first places in some of the initial percentages cycle: around 20% and 30%. Note how ASM decreases its performance in systole reaching third and fourth places in the subsequent phases compared to the initial percentages 0% and 10% of the cardiac cycle. FLS/HCs also has a satisfactory performance considering that FLS did not converge on epicardium segmentation. The best results were achieved with ASM, ASM/QHCs, ASM/LBP, and FLS/HCs. Two of these methods include information from the HCs. No previous training is required regarding FLSs-based approaches, so they have a substantial advantage over the other methods especially in time and computational work.

7. Conclusions and future work

In this research, we implemented a semi-automatic segmentation method for the left ventricle on the short axis view throughout the cardiac cycle. Due to limitations of the tissue reproduction in CT images, we tested various approaches and explored the performance of two types of
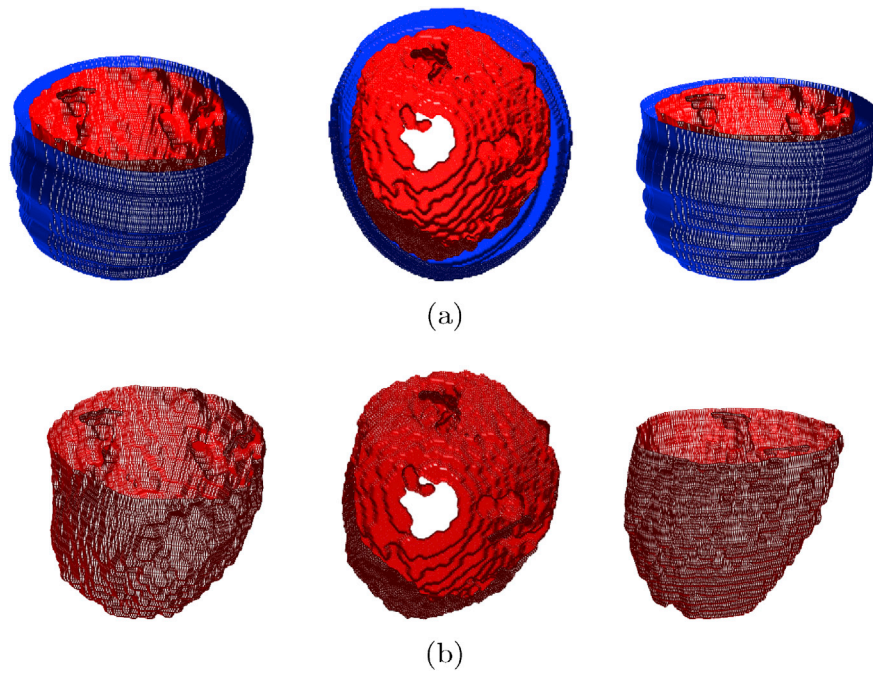
Fig. 14. Volume segmentation of endocardium (red) and epicardium (blue) in (a) and only the endocardium in (b) using FLS/HCs. (For interpretation of the references to colour in this figure legend, the reader is referred to the web version of this article.)
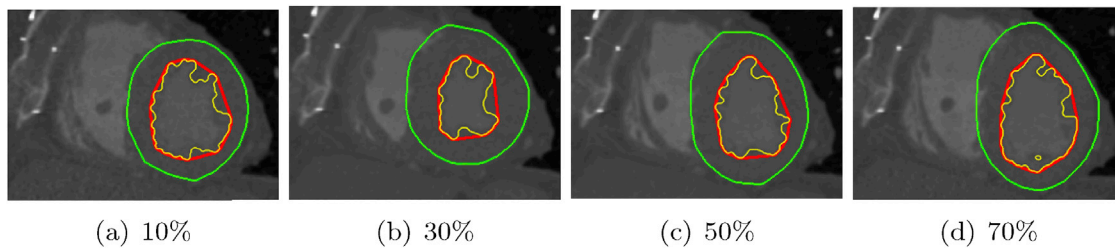

(a) 10%   (b) 30%   (c) 50%   (d) 70%

Fig. 15. Segmentation of endocardium (red), epicardium (green) and papillary muscles (yellow) of a patient with infarction, using FLS/HCs at different percentages of the cardiac cycle. (For interpretation of the references to colour in this figure legend, the reader is referred to the web version of this article.)

deformable models: Active shape models and level sets. The main contribution of this article is the inclusion of Hermite features and texture descriptors to improve the segmentation performance, especially when we deal with noisy images and lack of contrast. The segmentation of the left ventricle presented in this work constitutes an innovative method for understanding complex heart dynamics. The results obtained resemble clinical delineations in CT imaging and prove that the methods proposed here may help to reduce bias in diagnosis and treatment procedures. We showed that the joint approach FLS/HCs is a reliable option for segmenting LV, because it is able to differentiate between endocardium and epicardium borders. Another advantage of this approach is the fact that it does not need previous training.

In the last part of this paper, we introduce a novel method to assess contour-based segmentation called Ray Feature error. The results provided by Ray Feature error in epicardium and endocardium segmentation are consistent with the results provided by Dice index and Hausdorff distance (see Figs. 10 and 11). In addition, we present two synthetic cases where Dice index and Hausdorff distance fail, whereas Ray Feature error rates segmentation performance in a better way. Ray Feature error represents a simple way to estimate segmentation error in a range $[0, 1]$. Since the error is anywhere between zero and one, it gives an estimation of its magnitude. RFE measures errors along a circular path using discrete

steps; therefore, it is also suited to measure segmentation errors on directions of specific interest.

Future work should design the best strategy to be tested on patients with heart pathologies and 3D implementation with optimum methodology. Also further analysis must be conducted to obtain quantitative parameters of the LV such as ejection fraction that is essential for medical diagnosis.

Conflict of interest

None of the authors has any conflict of interest. The authors have no personal financial or institutional interest in any of the materials, software or devices described in this article.

Acknowledgments

A. Ray Feature error

Since active contours have become a popular technique frequently used in image segmentation, it is necessary to use a metric that assesses their performance objectively. Here, we propose a fast and solid yet simple method for quantitative evaluation of contour-based segmentation called Ray Feature error (RFE) (see Fig. 16). RFE is based on the original proposal of ray features [49] where the authors computed four image features to characterize irregular shapes: distance difference, distance feature, orientation, and norm feature.
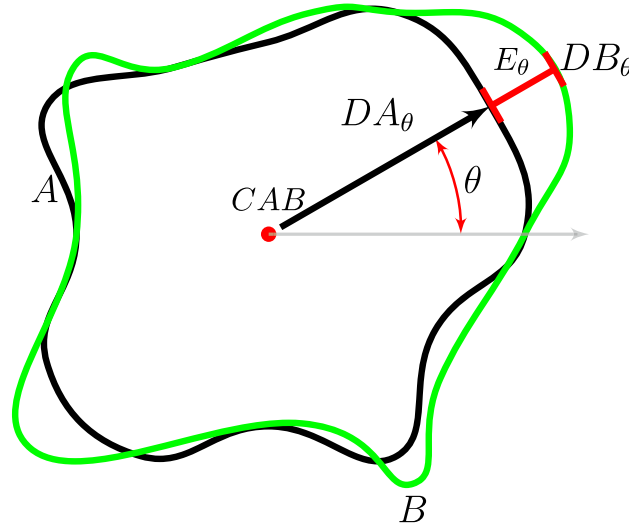

Fig. 16. Ray Feature error (RFE). Given two closed overlapping objects, RFE measures similarities between them by computing and adding E_θ with $\theta = \{0, \ldots, 2\pi\}$.

RFE permits the measurement of shape similarities between two overlapping objects as follows:

- Given two closed objects A and B, we define the location C_{AB} as the common centroid of both objects.
- It is possible to calculate the distance from the location p in A to the nearest border in the direction of θ as follows:

$$dA_\theta(p, \theta) = ||f(A, p, \theta) - p|| \tag{10}$$

where $f(A, p, \theta)$ returns to the location of the nearest border to p in A in the direction of θ and $\| \bullet \|$ is the Euclidean norm.

- The local error between two objects in the direction of θ is obtained as the absolute value of the difference amongst the distances:

$$E(AB)_\theta = \left| dA_\theta - dB_\theta \right| \tag{11}$$

- Finally, RFE is computed as:

$$RFE(A, B) = \frac{\sum_\theta \left| dA_\theta - dB_\theta \right|}{DA + DB} \tag{12}$$

where $DX = \sum dX_\theta$.

RFE represents a simple and fast way to compare two overlapping closed shapes. It varies within the range $[0, \ 1)$ and $RFE(A, B) = 0$ if and only if A and B have the closure, $A = B$.

A.1. Metric comparison

Although many methods for left ventricle segmentation have been developed during recent years, the majority of the heart segmentation methods in the literature remain difficult to compare. Furthermore, one of the difficulties when working with medical imaging is the large inter-observer variability even when the observers are considered to be experts.

An objective evaluation is a crucial step to ascertain if the results are acceptable from a medical point of view and is intended to indicate the degree of reliability of the method. Thus, a relevant evaluation method must be able to detect small differences between two segmentation procedures.

Dice index (DI) belongs to a class of region-based evaluation methods and is defined as twice the intersection of two sets X and Y divided by the sum of the cardinality of the two sets, as follows:

$$DI = \frac{2|X \cap Y|}{|X| + |Y|} \tag{13}$$

DI is equal to 1 when the two sets are exactly the same, and 0 when the two sets are completely different. However, since it is a metric based on areas, a limitation of this criterion is that several segmentations can arrive at the same result, see Fig. 17.
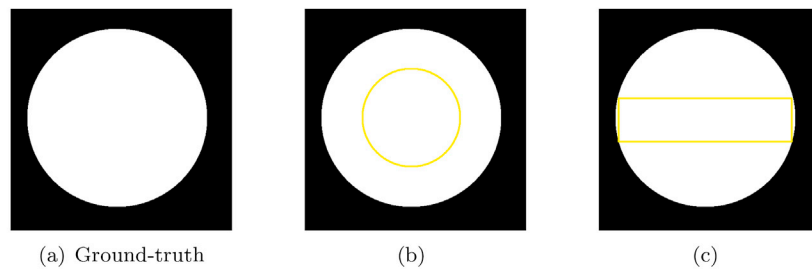
(a) Ground-truth   (b)   (c)

Segmentation comparison of synthetic shapes. Ground truth is in white and segmentations in yellow. Regions within yellow contours are different in shape but have the same area. Note that in this case, Dice index is not a suitable criterion because the index is the same in both cases.

Method	(b)	(c)
Ray Feature Error	**0.2927**	0.3529
Hausdorff distance	**104.6614**	160
Dice index	0.4588	0.4588

Fig. 17. Two examples of segmentation. Bold values represent the best results and letters in parentheses represent the corresponding case.

On the other hand, Hausdorff distance (HD) is a standard metric that measures the distance between two contours A and B. The measurement is the maximum distance among all the minimum distances between A and B. Hausdorff represents a pseudo-distance because $HD(A, B) \neq HD(B, A)$. It therefore, computes the distances twice and since it only considers a maximum value, it is sensitive to local variations, see Fig. 18. Another disadvantage is that the measurement is not bounded so we cannot easily estimate the performance of a segmentation.

(a) Ground-truth   (b)   (c)
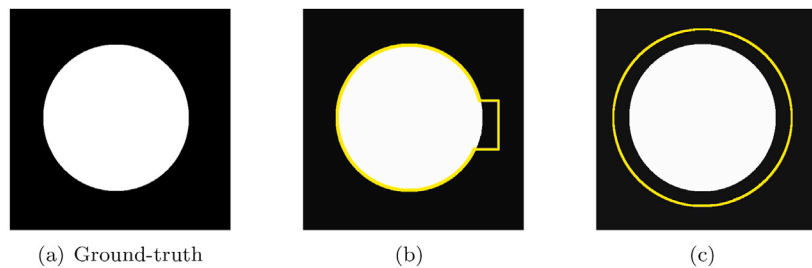
Summary of contour comparisons. Since Hausdorff distance is define as the maximum of the minimum distances between two sets of points, it fails in this example. Bold values represent better results. Letters in parentheses represent the corresponding case.

Method	(b)	(c)
Ray feature error	**0.0246**	0.0990
Hausdorff distance	39.0128	39.0128
Dice index	**0.9737**	0.8026

Fig. 18. Two examples of segmentation with the ground-truth in white and the resulted segmentations in yellow. Note that in both cases, Hausdorff distance is the same.

We believe our proposal Ray Feature error reflects the quality of the segmentation better and overcomes the previous issues related with DI and HD. Furthermore, it is a real distance and is bounded $[0, 1)$ where 0 represents perfect segmentation. Therefore we can achieve a more accurate understanding of the performance of the segmentation.

Appendix A. Supplementary data

Supplementary data related to this article can be found at http://dx.doi.org/10.1016/j.compbiomed.2017.05.025.

References

[1] World Health Organization (WHO), Cardiovascular Diseases (CVDs), Fact Sheet, accessed: 2016-04-20, 2015. URL, http://www.who.int/mediacentre/factsheets/fs317/en/.

[2] S. Ye, Acute myocardial infarction, in: M.D. Gellman, J.R. Turner (Eds.), Encyclopedia of Behavioral Medicine, Springer, New York, 2013, pp. 27–29, http://dx.doi.org/10.1007/978-1-4419-1005-9_1243.

[3] Centers for Disease Control and Prevention, Heart Failure Fact Sheet, accessed: 2017-01-12, 2016. URL, https://www.cdc.gov/dhdsp/data_statistics/fact_sheets/fs_heart_failure.htm.

[4] D. Mozaffarian, E.J. Benjamin, A.S. Go, D.K. Arnett, M.J. Blaha, M. Cushman, S.R. Das, S. de Ferranti, J.-P. Després, H.J. Fullerton, V.J. Howard, M.D. Huffman, C.R. Isasi, M.C. Jiménez, S.E. Judd, B.M. Kissela, J.H. Lichtman, L.D. Lisabeth, S. Liu, R.H. Mackey, D.J. Magid, D.K. McGuire, E.R. Mohler, C.S. Moy, P. Muntner, M.E. Mussolino, K. Nasir, R.W. Neumar, G. Nichol, L. Palaniappan, D.K. Pandey, M.J. Reeves, C.J. Rodriguez, W. Rosamond, P.D. Sorlie, J. Stein, A. Towfighi, T.N. Turan, S.S. Virani, D. Woo, R.W. Yeh, M.B. Turner, Heart Disease and Stroke Statistics—2016 Upyear, 2016, http://dx.doi.org/10.1161/CIR.0000000000000350. URL, http://circ.ahajournals.org/content/133/4/e38.

[5] T.C. Wong, P. Soman, Imaging in the evaluation of the patient with new-onset heart failure, Curr. Cardiovasc. Imaging Rep. 5 (3) (2012) 167–172, http://dx.doi.org/10.1007/s12410-012-9136-6.

[6] R. Ventura-Clapier, Encyclopedia of Exercise Medicine in Health and Disease, Springer Berlin Heidelberg, 2012, http://dx.doi.org/10.1007/978-3-540-29807-6_4103. Ch. Cardiomyopathies, pp. 175–175.

[7] S. Leschka, S. Waelti, S. Wildermuth, Principles of CT imaging, in: F. Saremi (Ed.), Cardiac CT and MR for Adult Congenital Heart Disease, Springer, 2014, pp. 77–105.

[8] D. Kang, J. Woo, P.J. Slomka, D. Dey, G. Germano, C.-C. Jay Kuo, Heart chambers and whole heart segmentation techniques: Review, J. Electron. Imaging 21 (1) (2012), 010901–1–010901–16.

[9] K. Moschetti, S. Muzzarelli, C. Pinget, A. Wagner, G. Pilz, J. Wasserfallen, J. Schulz-Menger, D. Nothnagel, T. Dill, H. Frank, M. Lombardi, O. Bruder, H. Mahrholdt, J. Schwitter, Cost evaluation of cardiovascular magnetic resonance versus coronary angiography for the diagnostic work-up of coronary artery disease: application of the European Cardiovascular Magnetic Resonance registry data to the German, United Kingdom, Swiss, and United States health care systems, J. Cardiovasc. Magn. Reson. 14 (1) (2012) 35, http://dx.doi.org/10.1186/1532-429X-14-35.

[10] S. Halliburton, A. Arbab-Zadeh, D. Dey, A.J. Einstein, R. Gentry, R.T. George, T. Gerber, M. Mahesh, W.G. Weigold, State-of-the-art in CT hardware and scan modes for cardiovascular CT, J. Cardiovasc. Comput. Tomogr. 6 (3) (2012) 154–163, http://dx.doi.org/10.1016/j.jcct.2012.04.005.

[11] U.J. Schoepf, C.R. Becker, L.K. Hofmann, Y.E. Kent, Multidetector-row CT of the heart, Radiol. Clin. 42 (3) (2004) 635–649, http://dx.doi.org/10.1016/j.rcl.2004.03.011.

[12] R. Fischbach, Cardiac and cardiothoracic anatomy in CT, in: B. Ohnesorge, T. Flohr, C. Becker, A. Knez, M. Reiser (Eds.), Multi-slice and Dual-source CT in Cardiac Imaging, Springer Berlin Heidelberg, 2007, pp. 23–39, http://dx.doi.org/10.1007/978-3-540-49546-8_2.

[13] C. Petitjean, J.-N. Dacher, A review of segmentation methods in short axis cardiac MR images, Med. Image Anal. 15 (2) (2011) 169–184.

[14] X. Bresson, S. Esedoglu, P. Vandergheynst, J.-P. Thiran, S. Osher, Fast global minimization of the active contour/snake model, J. Math. Imaging Vis. 28 (2) (2007) 151–167, http://dx.doi.org/10.1007/s10851-007-0002-0.

[15] Y.-L. Lu, K. A. Connelly, A. J. Dick, G. A. Wright, P. E. Radau, Automatic functional analysis of left ventricle in cardiac cine MRI, Quant. Imaging Med. Surg. 3(4).

[16] D. Turco, C. Corsi, Series in Computer Vision in Medical Imaging. Computer Vision, Advanced PDE-based Methods for Automatic Quantification of Cardiac Function and Scar from Magnetic Resonance Imaging, 2, World Scientific Publishing Company, 2013.

[17] A.V. Juan, J. Cerrolaza, R. Cabeza, Series in Computer Vision in Medical Imaging. Computer Vision, On Hierarchical Statistical Shape Models with Application to Brain MRI, 2, World Scientific Publishing Company, 2013.

[18] A. Kronman, L. Joskowicz, A geometric method for the detection and correction of segmentation leaks of anatomical structures in volumetric medical images, Int. J. Comput. Assist. Radiol. Surg. 11 (3) (2016) 369–380, http://dx.doi.org/10.1007/s11548-015-1285-z.

[19] M.N. Bugdol, E. Pietka, Mathematical model in left ventricle segmentation, Comput. Biol. Med. 57 (C) (2015) 187–200.

[20] J. Kawa, E. Pietka, Kernelized fuzzy c-means method in fast segmentation of demyelination plaques in multiple sclerosis, in: 29th International Conference of the IEEE Engineering in Medicine and Biology Society, IEEE, 2007, pp. 5616–5619, http://dx.doi.org/10.1109/iembs.2007.4353620.

[21] F. Ma, J. Liu, B. Wang, H. Duan, Automatic segmentation of the full heart in cardiac computed tomography images using a haar classifier and a statistical mode, J. Med. Imaging Health Inf. 6 (5) (2016) 1298–1302, http://dx.doi.org/10.1166/jmihi.2016.1916.

[22] J. Dolz, H.A. Kirişli, T. Fechter, S. Karnitzki, O. Oehlke, U. Nestle, M. Vermandel, L. Massoptier, Interactive contour delineation of organs at risk in radiotherapy: clinical evaluation on NSCLC patients, Med. Phys. 43 (5) (2016) 2569–2580, http://dx.doi.org/10.1118/1.4947484.

[23] S. Antunes, A. Esposito, A. Palmisano, C. Colantoni, S. Cerutti, G. Rizzo, Cardiac multi-detector CT segmentation based on multiscale directional edge detector and 3D level set, Ann. Biomed. Eng. 44 (5) (2016) 1487–1501, http://dx.doi.org/10.1007/s10439-015-1422-4.

[24] J. Keomany, S. Marcel, Active Shape Models Using Local Binary Patterns, Tech. rep., IDIAP, 2006.

[25] J. Olveres, R. Nava, E. Moya-Albor, B. Escalante-Ramírez, J. Brieva, G. Cristóbal, E. Vallejo, Texture descriptor approaches to level set segmentation in medical images, in: Proc. SPIE Europe, 9138, 2014, http://dx.doi.org/10.1117/12.2054527, 91380J–1–91380J–12.

[26] A. Estudillo-Romero, B. Escalante-Ramírez, Rotation-invariant texture features from the steered Hermite transform, Pattern Recognit. Lett. 32 (16) (2011) 2150–2162.

[27] J.-B. Martens, The Hermite transform-theory, IEEE Trans. Acoust. Speech Signal Process. 38 (9) (1990) 1595–1606.

[28] J.-B. Martens, The Hermite transform-applications, IEEE Trans. Acoust. Speech Signal Process. 38 (9) (1990) 1607–1618.

[29] Y. Wu, J. Shen, Properties of orthogonal Gaussian-Hermite moments and their applications, EURASIP J. Adv. Signal Process. 2005 (4) (2005) 1–12, http://dx.doi.org/10.1155/ASP.2005.588.

[30] C.J. Rivero-Moreno, S. Bres, Texture feature extraction and indexing by Hermite filters, in: Proceedings of the 17th International Conference on Pattern Recognition, 1, 2004, pp. 684–687, http://dx.doi.org/10.1109/ICPR.2004.1334266.

[31] J.W. Weinsaft, M.D. Cham, M. Janik, J.K. Min, C.I. Henschke, D.F. Yankelevitz, R.B. Devereux, Left ventricular papillary muscles and trabeculae are significant determinants of cardiac MRI volumetric measurements: effects on clinical standards in patients with advanced systolic dysfunction, Int. J. Cardiol. 126 (3) (2008) 359–365, http://dx.doi.org/10.1016/j.ijcard.2007.04.179.

[32] T.F. Cootes, C.J. Taylor, D.H. Cooper, J. Graham, Active shape models: their training and application, Comput. Vis. Image Underst. 61 (1) (1995) 38–59, http://dx.doi.org/10.1006/cviu.1995.1004.

[33] T.F. Cootes, G.J. Edwards, C.J. Taylor, Active appearance models, in: H. Burkhardt, B. Neumann (Eds.), 5th European Conference on Computer Vision, Proceedings, II, Springer Berlin Heidelberg, 1998, pp. 484–498, http://dx.doi.org/10.1007/BFb0054760.

[34] Y. Hum, Segmentation of Hand Bone for Bone Age Assessment, SpringerBriefs in Applied Sciences and Technology, Springer Singapore, 2013.

[35] T. Chan, L. Vese, Active contours without edges, IEEE Trans. Image Process. 10 (2) (2001) 266–277, http://dx.doi.org/10.1109/83.902291.

[36] T.F. Chan, B.Y. Sandberg, L.A. Vese, Active contours without edges for vector-valued images, J. Vis. Commun. Image Represent. 11 (2000) 130–141.

[37] C. Li, C. Kao, J. Gore, Z. Ding, Implicit active contours driven by local binary fitting energy, in: IEEE Conference on Computer Vision and Pattern Recognition (CVPR), 2007, pp. 1–7.

[38] B.X. Houhou Nawal, Jean-Philippe Thiran, Fast texture segmentation based on semi-local region descriptor and active contour, Numer. Math. Theory Methods Appl. 2 (2009) 445–468.

[39] J. Kratky, J. Kybic, Three-dimensional segmentation of bones from CT and MRI using fast level sets, in: Proc. SPIE Medical Imaging, 6914, 2008, 691447–1–691447–10.

[40] C. Xu, D.L. Pham, J.L. Prince, Image segmentation using deformable models, in: Handbook of Medical Imaging, 2, SPIE, 2009, pp. 175–272. Medical Image Processing and Analysis.

[41] T. Lindeberg, A computational theory of visual receptive fields, Biol. Cybern. 107 (6) (2013) 589–635, http://dx.doi.org/10.1007/s00422-013-0569-z.

[42] R. Young, R. Lesperance, W.W. Meyer, The Gaussian derivative model for spatial-temporal vision: I. Cortical model, Spat. Vis. 14 (3) (2001) 261–319, http://dx.doi.org/10.1163/156856801753253582.

[43] J.L. Silván-Cárdenas, B. Escalante-Ramírez, The multiscale Hermite transform for local orientation analysis, IEEE Trans. Image Process. 15 (5) (2006) 1236–1253.

[44] M.D. Cerqueira, N.J. Weissman, V. Dilsizian, A.K. Jacobs, S. Kaul, W.K. Laskey, D.J. Pennell, J.A. Rumberger, T. Ryan, M.S. Verani, Standardized myocardial segmentation and nomenclature for tomographic imaging of the heart, Circulation 105 (4) (2002) 539–542, http://dx.doi.org/10.1161/hc0402.102975.

[45] P.M.B. Natalia, A. Trayanova, Cardiac arrhythmias: mechanistic knowledge and innovation from computer models, in: M.D. Gellman, J.R. Turner (Eds.), Modeling the Heart and the Circulatory System, 14, Springer International Publishing, 2015, pp. 27–29, http://dx.doi.org/10.1007/978-3-319-05230-4.

[46] J. Olveres, R. Nava, B. Escalante-Ramírez, G. Cristóbal, C.M. García-Moreno, Midbrain volume segmentation using active shape models and LBPs, in: Proc. SPIE Europe, 8856, 2013, 88561F–1–88561F–11.

[47] R. Nava, G. Cristóbal, B. Escalante-Ramírez, A comprehensive study of texture analysis based on local binary patterns, in: Proc. SPIE 8436, Optics, Photonics, and Digital Technologies for Multimedia Applications II, 2012, http://dx.doi.org/10.1117/12.923558, 84360E–1–84360E–12.

[48] O. Pele, M. Werman, The quadratic-chi histogram distance family, in: Computer Vision – ECCV 2010: 11th European Conference on Computer Vision, Proceedings, Part II, Springer Berlin Heidelberg, 2010, pp. 749–762, http://dx.doi.org/10.1007/978-3-642-15552-9_54.

[49] K. Smith, A. Carleton, V. Lepetit, Fast ray features for learning irregular shapes, in: IEEE 12th International Conference on Computer Vision, 2009, pp. 397–404, http://dx.doi.org/10.1109/ICCV.2009.5459210.

Jimena Olveres received a Bachelor of Biomedical Engineering degree from the Universidad Iberoamericana A.C., a Master of Electrical Engineering degree and is a Ph.D. candidate at the Posgrado en Ciencia e Ingeniería en Computación from the Universidad Nacional Autónoma de México. She has been lecturing on medical image processing and computer vision at the Electrical Engineering Division of the School of Engineering. Her research interests are in computer vision, image processing, and segmentation.

Rodrigo Nava was born in Mexico City. He obtained the Bachelor of Computer Engineering degree in 2004; the Master of Computer Science and Engineering degree in 2007; and the Doctor of Engineering degree in 2013, all with honors, from the Universidad Nacional Autónoma de México. His research interests include bio-inspired image models, image fusion, image quality, and wavelets. He is a Candidate Member of the National Research System (CONACYT: 2015–2017).

Boris Escalante-Ramírez received a Bachelor of Electrical Engineering degree from Universidad Nacional Autónoma de México in 1985, a Master of Electronic Engineering degree from the Philips International Institute of Technological Studies, Eindhoven, The Netherlands, in 1987, and a Ph.D. degree from the Eindhoven University of Technology in

1992. Since then he has been with the Electrical Engineering Division of the School of Engineering, Universidad Nacional Autónoma de México.

Enrique Vallejo was born in Mexico City. He holds an M.D degree from Universidad Nacional Autónoma de México. He has medical specialties on General internal medicine, Cardiology, Nuclear cardiology and Positron emission tomography and Cardiac tomography.

Jan Kybic received the Master's degree from the Czech Technical University in Prague, Czech Republic and the PhD degree from EPFL, Switzerland, in 1998 and 2001, respectively. He held a postdoc position at INRIA, France, in 2002–2003. Since 2003, he has been at Czech Technical University in Prague, becoming an associate professor in 2010 and currently serving as a department head. He was a visiting researcher at EPFL for his sabbatical in 2010. He has authored or coauthored 21 articles in peer-reviewed international scientific journals, one book, two book chapters, and more than 60 conference publications. He has supervised 10 PhD students, five of them have already successfully graduated. He is an associate editor for the IEEE Transactions on Medical Imaging. His current research interests include algorithms for biomedical signal and image processing, especially image registration, segmentation and classification, numerical methods, interpolation, inverse problems, and algorithm theory.